

The Thermal Structure of Gravitationally-Darkened Classical Be Star Disks

M. A. McGill¹, T. A. A. Sigut¹, & C. E. Jones¹,

ABSTRACT

The effect of gravitational darkening on models of the thermal structure of Be star disks is systematically studied for a wide range of Be star spectral types and rotation rates. Gravitational darkening causes a reduction of the stellar effective temperature towards the equator and a redirection of energy towards the poles. It is an important physical effect in these star-disk systems because the photoionizing radiation from the central B star is the main energy source for the disk. We have added gravitational darkening to the BEDISK code to produce circumstellar disk models that include both the variation in the effective temperature with latitude and the non-spherical shape of the star in the calculation of the stellar photoionizing radiation field. The effect of gravitational darkening on global measures of disk temperature is generally significant for rotation rates above 80% of critical rotation. For example, a B0V model rotating at 95% of critical has a density-averaged disk temperature ≈ 2500 K cooler than its non-rotating counterpart. However, detailed differences in the temperature structure of disks surrounding rotating and non-rotating stars reveal a complex pattern of heating and cooling. Spherical gravitational darkening, an approximation that ignores the changing shape of the star, gives good results for disk temperatures for rotation rates less than $\approx 80\%$ of critical. However for the highest rotation rates, the distortion of the stellar surface caused by rotation becomes important.

Subject headings: stars: circumstellar matter – stars: emission line, Be
– stars: rotation

¹Department of Physics and Astronomy, The University of Western Ontario, London, Ontario, N6A 3K7, Canada

1. Introduction

A classical Be-star is a non-supergiant B star that possesses a gaseous equatorial disk (Porter & Rivinus 2003). This circumstellar material produces an emission line spectrum including a prominent $H\alpha$ emission line. Some Be stars, for example γ Cassiopeia, produce a rich emission line spectrum with many hydrogen lines and some metal lines. Be star disks also produce a continuum excess due to bound-free and free-free emission. This excess has been observed at a variety of wavelengths from the visible to the radio (Coté & Waters 1987; Waters & Coté 1987). Linear polarization of up to 2% has been observed in the continuum emission and is caused by electron scattering in the non-spherical circumstellar envelope (McLean & Brown 1978; Poeckert et al. 1979). Be star disks have been partially resolved by long-baseline interferometric measurements, initially in the radio (Dougherty & Taylor 1992), and later at infrared and optical wavelengths (Stee & Bittar 2001; Tycner 2004).

The stellar absorption lines of Be stars indicate rapid rotation of the central star, and this property is thought to play an important role in the release of material into the disk (Porter 1996). There is strong evidence that Be star disks are in Keplerian rotation (Hummel & Vrancken 2000; Oudmaijer et al. 2008); however, it is still uncertain if the equatorial rotation speeds of Be stars are close to “critical”, i.e. close to the Keplerian orbital speed at the inner edge of the disk (Cranmer 2005). In addition, another mechanism must somehow allow for the wide range of behaviours observed in Be stars: some systems have exhibited essentially stable $H\alpha$ emission for as long as they have been observed, while others are highly variable with timescales ranging from less than a day to decades (Porter & Rivinus 2003).

A rapidly rotating star is changed in two ways: the stellar surface is distorted with the equatorial radius becoming larger than the polar radius, and the stellar surface temperature acquires a dependence on stellar latitude with cooler gas at the equator compared to the hotter pole. These phenomena together are commonly called gravitational darkening. The rotational distortion and surface intensity variation with latitude have direct observational support from interferometric observations, including the stars Achernar (Domiciano de Souza et al. 2003) and Altair (Monnier et al. 2007).

Because the equatorial region of the photosphere is both the fastest rotating and the dimmest, it can be difficult to detect this maximally Doppler-shifted region in integrated light. This problem can be compounded by the obscuration of the equatorial regions by disk material. As a result, the bounds on Be star rotation rates remain contentious (Chauville et al. 2001; Townsend et al. 2004; Cranmer 2005; Fremat et al. 2005). Nevertheless, the canonical result is that most Be stars rotate at $\approx 80\%$ of their critical speed (as defined in Section 2). Unfortunately, it seems that directly measuring projected rotational

velocities above 80% of the critical speed may not be possible due to the dimming of the equatorial regions (Townsend et al. 2004). Cranmer (2005) presents a detailed statistical analysis of Be star $v \sin i$ values in which he attempts to match the observed distributions using a parametrized distribution of equatorial velocities. He concludes that early-type Be stars, O7–B3.5, must rotate at rates significantly less than their critical speeds (peaking at 40-60%) while later type Be stars, B3.5–A0, rotate much closer to their critical speeds (peaking at 70-90%).

Previously, the effects of gravitational darkening have been included in disk models for the stars Achernar, or α Eridani, (Carciofi et al. 2008) and ζ Tauri (Carciofi et al. 2009). However, the rotating star was assumed to be a spheroid rather than following a Roche profile (see Section 2). In the literature, gravitational darkening has been included only as a fit parameter in models of individual stars. A comprehensive study on the how the inclusion of gravitational darkening affects models of Be star disks has not yet been performed.

In this paper, we systematically examine the effect of gravitational darkening on the thermal structure of a circumstellar disk. We restrict our investigation to changes in the energy reaching the disk and the resulting changes in the temperature distribution. Section 2 outlines the basic theory behind gravitational darkening and also gives computational details. Section 3 describes the stellar and disk models chosen for this investigation. Results are presented in Section 4 where the consequences of rotation on the energy reaching the circumstellar disk (Section 4.1) and the corresponding changes in the disk temperature structure (Section 4.2) are investigated. In Section 5, we examine the two principle ingredients of gravitational darkening (temperature variation with latitude and distortion of the stellar surface) separately in order to gauge their relative importance. We also evaluate the effectiveness of the simpler spherical gravitational darkening approximation in which the shape distortion produced by rapid rotation is ignored. Section 6 gives the conclusions, and in Appendix A, we discuss the subtle aspect of how varying the equatorial radius can change the inherent properties of our disk models.

2. Theory of Gravitational Darkening

2.1. The Central Star

Gravitational darkening, first described by von Zeipel (1924), is due to a rotational, centrifugal term included in the classical gravitational potential. For a star rotating at a

fixed angular speed ω , the potential, Φ , in spherical coordinates (r, θ, ϕ) , is given by

$$\Phi(r, \theta) = -\frac{GM}{r} - \frac{1}{2}\omega^2 r^2 \sin^2 \theta, \quad (1)$$

where G is the gravitational constant, M is the stellar mass, and θ is the stellar co-latitude ($\theta = 0^\circ$ on the polar axis). The local gravitational acceleration is given by

$$\vec{g}(\theta) = \left(\omega^2 r \sin^2 \theta - \frac{GM}{r^2} \right) \hat{r} + (\omega^2 r \sin \theta \cos \theta) \hat{\theta}. \quad (2)$$

The angular speed at which the local value of gravity at the equator becomes zero defines the critical angular speed, ω_{crit} , and the corresponding critical rotation velocity, v_{crit} . The angular speeds and the equatorial velocities of stars are often expressed as fractions of these critical values, ω_{frac} and v_{frac} . The relevant equations are

$$\begin{aligned} \omega_{\text{crit}} &= \sqrt{\frac{8GM}{27r_p^3}}, & \omega_{\text{frac}} &\equiv \frac{\omega}{\omega_{\text{crit}}}, \\ v_{\text{crit}} &= \sqrt{\frac{2GM}{3r_p}}, & v_{\text{frac}} &\equiv \frac{v_{\text{eq}}}{v_{\text{crit}}}, \end{aligned} \quad (3)$$

where r_p is the polar radius of the star. In our calculations we have assumed that the polar radius remains constant following Collins (1966).

By requiring the potential across the surface to be constant, the radius as a function of θ is found to be (see again Collins 1966)

$$r(\theta) = \left(\frac{-3r_p}{\omega_{\text{frac}} \sin \theta} \right) \cos \left(\frac{\arccos(\omega_{\text{frac}} \sin \theta) + 4\pi}{3} \right). \quad (4)$$

When the equator of the star becomes unbound at $\omega = \omega_{\text{crit}}$, $r(\theta = \frac{\pi}{2})$ takes on its largest value, $\frac{3}{2}r_p$. The Roche distortion of a stellar surface has direct interferometric confirmation. For example, Zhao et al. (2010) present reconstructed images of α Cep and α Oph which clearly reveal rotational distortion consistent with the von Zeipel theory. The shape of the distorted surface affects the stellar radiation intercepted by the disk as the mid-latitudes are tipped towards the pole and away from the equatorial regions. In addition, rapid rotation increases the surface area and projected surface area of the star. The physical effects associated with near critical rotation have been recently reviewed by Meynet et al. (2010).

The local effective temperature of the stellar atmosphere, T_{eff} , and the local surface gravity, $|\vec{g}|$, are related by von Zeipel's theorem,

$$T_{\text{eff}}(\theta) = (C_\omega |\vec{g}(\theta)|)^{1/4}, \quad (5)$$

where C_ω is von Zeipel’s constant. Vinicius et al. (2007) find that the von Zeipel variation of T_{eff} with stellar latitude is required to simultaneously fit several HeI photospheric absorption profiles from five rapidly rotating, early-type Be stars. Nevertheless, the power of 1/4 appearing in the standard gravity-darkening law has been observationally questioned by Monnier et al. (2007) who find a better fit to their interferometric observations of Altair with an exponent of 0.19 ± 0.012 . van Belle (2010) reviews all current interferometric observations of rapidly rotating stars and finds that of six observed stars, four are well fit by the standard 1/4 exponent and two (including Altair) are not. Despite these results, we will retain the standard exponent in all calculations to follow.

The constant, C_ω , is defined using the assumption that the total luminosity of the star remains fixed (for discussion of this point, see Lovekin et al. 2006). Therefore, while the equatorial temperature of a star decreases with rotation rate, the polar temperature must increase to maintain a constant luminosity. This effect is illustrated in Figure 1 which shows the change in temperature with increasing rotation for five stellar co-latitudes: 0° , 30° , 60° , 70° , and 90° . In the absence of rotation, the stellar surface has a uniform temperature, but as the rotation speed increases the surface temperatures begin to diverge. Note that the temperatures of the middle co-latitudes, such as 60° , do not monotonically increase or decrease in temperature. For example as rotation increases from zero, the temperature at 60° decreases until $\sim 0.80 v_{\text{crit}}$ where it reaches a minimum before increasing slightly with increased rotation.

The constant C_ω can be found for a specific set of stellar parameters (r_p , M and L), given a value of ω , by integrating the local gravity over the stellar surface and then multiplying by the luminosity divided by the Stephan-Boltzmann constant. Once C_ω has been determined for one set of stellar parameters, the results can be rescaled for any other star following Collins (1966) using

$$C'_\omega C_\omega = \frac{ML'}{M'L} . \quad (6)$$

Here M' , L' , & C'_ω are the mass, luminosity and von Zeipel’s constant of a particular star, and M , L , & C_ω are for another star with an identical rotation rate.

The local gravity and surface orientation can be established from Equation 2, and the temperature from Equation 5. This allows the properties of the local stellar atmosphere, g and T_{eff} , to be defined for each point on the surface of the star.

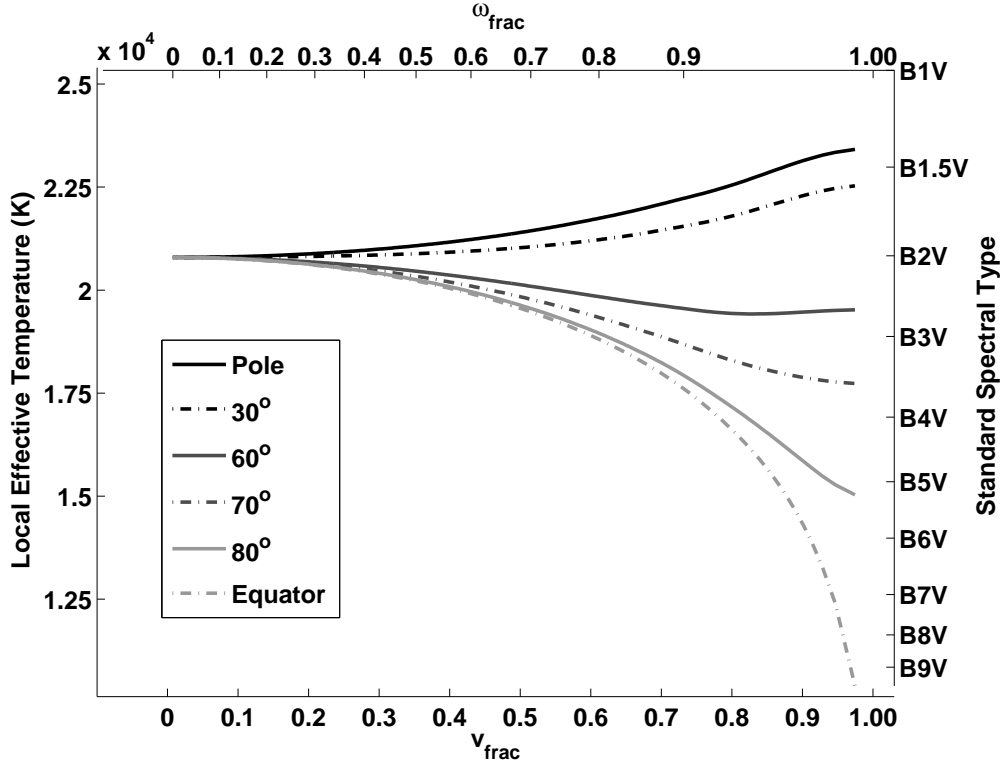


Fig. 1.— Change in the local effective temperature with increasing v_{frac} (lower axis) for a B2V stellar model (see Table 1). The upper axis shows the corresponding ω_{frac} . The darkest solid line gives the polar temperature ($\theta = 0^\circ$), while the lightest grey dash-dot line shows the equatorial temperature ($\theta = 90^\circ$). Various intermediate stellar latitudes are also shown. The right vertical axis shows the standard main sequence spectral type (with no rotation) for the same surface temperature as the left axis (Cox 2000).

2.2. The Circumstellar Disk

We now turn to the Be star circumstellar disk. From a particular vantage point within the disk, labelled \vec{s} , defined using the cylindrical coordinates, (s_R, s_z, s_Φ) , only a portion of the star is visible. For a section of the stellar surface specified by $\vec{r}(\theta, \phi)$ to be visible from the vantage point, the dot product between the unit vector pointing from the stellar surface to the vantage point, $\hat{n}_{\text{vp}} = \frac{\vec{s}-\vec{r}}{|\vec{s}-\vec{r}|}$, and the local surface normal, $\hat{n}_{\text{surf}} = \frac{-\vec{g}_\theta}{|g_\theta|}$, must be greater than zero. The boundary of this region where $\hat{n}_{\text{surf}} \cdot \hat{n}_{\text{vp}} = 0$ is important because it allows the lines of sight between the star and the vantage point to be efficiently chosen. The upper and lower edges of the visible region correspond to the maximum and minimum values of θ such that $\hat{n}_{\text{surf}} \cdot \hat{n}_{\text{vp}} \geq 0$. These are found by solving

$$\frac{8}{27}\omega_{\text{frac}}^2 \frac{r_\theta^3}{r_p^3} s_R \sin \theta - r_\theta - s_R \sin \theta + s_z \cos \theta = 0 \quad (7)$$

for its two solutions, θ_1 and θ_2 . For values of θ between θ_1 and θ_2 , the visible portion of the surface lies between the bounds on ϕ given by

$$\phi_{\text{edge}} = s_\Phi \pm \arccos \left(\frac{r(\theta) \sin^2 \theta (1 - \kappa_\theta) + r(\theta) \cos^2 \theta - s_z \cos \theta}{(s_R \sin \theta - \kappa_\theta s_R \sin \theta)} \right), \quad (8)$$

with

$$\kappa_\theta = \frac{8}{27}\omega_{\text{frac}}^2 \left(\frac{r_\theta}{r_p} \right)^3. \quad (9)$$

Given this geometry, we can now take into account the temperature changes and the radial distortion of the star to determine the photoionizing radiation field reaching each point in the disk. The effects of gravitational darkening are illustrated in Figure 2. This figure shows a star rotating at 80% of v_{crit} with its shape distortion and associated surface temperature variations. Figure 2 also shows the visible region, θ_1 , θ_2 and ϕ_{edge} , for a vantage point at a radius of $s_R = 2r_p$ and a height above the disk of $s_z = 1.2r_p$. The disk is assumed to be axisymmetric so any Φ dependence is not included. This figure demonstrates how the visible region changes from a simple spherical cap for a non-rotating star to an elongated region.

The circumstellar gas is exposed to photoionizing radiation from the various latitudes of the star and this radiation changes with increasing rotation. Different locations within the disk have different regions of the photosphere within their field of view. The polar temperature increases with rotation in contrast to the decrease in the equatorial temperature (see Figure 1). The drop in the equatorial temperature occurs at a faster rate than the rise in the polar temperature. This means the effects of the hot stellar pole become significant

at speeds above 80% of v_{crit} . In the equatorial plane up to a distance of $4r_p$, stellar latitudes above 25° are not visible for a circular star. For a critically rotating star this increases to $\approx 30^\circ$. As the gas density in the disk is assumed to fall off with height above the equatorial plane, the light reaching upper parts of the disk from the cooler stellar equatorial region passes through a greater optical depth than that from the hotter pole. Thus the effects of gravitational darkening can vary in strength depending on location within the disk and can have very different effects on the temperature depending on what part of the disk is considered. The effect of gravitational darkening cannot be considered to be simply a reduction of the effective temperature of the star.

3. Calculations

A gravitationally darkened version of BEDISK (Sigut & Jones 2007), incorporating the theory of Section 2, was created and run for the stellar parameters given in Table 1 and the rotation rates given in Table 2. These stellar parameters (adopted from Cox 2000) were chosen to include a model from four of the five bins used by Cranmer (2005) to analyze the effects of spectral type on Be star rotational statistics. For reasons discussed below, we have not considered models from the coolest bin (the bin with characteristic spectral type B8) considered by Cranmer (2005). BEDISK solves the statistical equilibrium equations for the atomic level population equations and then enforces radiative equilibrium at each point of the computational grid (Sigut & Jones 2007). The density structure of the disk is assumed to be of the form

$$\begin{aligned} \rho(R, z) &= \rho_o \left(\frac{R_*}{R} \right)^n e^{-(z/H)^2} , \\ H(R) &= \sqrt{\frac{2R^3 k T_{\text{iso}}}{GM\mu}} . \end{aligned} \tag{10}$$

Here R_* is the stellar radius (see next paragraph). In the second equation for the disk scale height, $H(R)$, μ is the mean-molecular weight of the gas, and T_{iso} is an assumed isothermal temperature used for the sole purpose of setting the density scale height. The models are constructed with the density parameters set to $n = 3$ and $\rho_o = 5 \times 10^{-11} \text{ g/cm}^3$. These density parameters are kept constant. The form of the disk density given by Equation 10 follows from the assumption of a radial power-law drop in the equatorial plane ($z = 0$) coupled with the assumption that the disk is in vertical hydrostatic equilibrium set by the z -component of the star's gravitational acceleration. Note that Equation 10 results in a flaring disk with $H \propto R^{3/2}$.

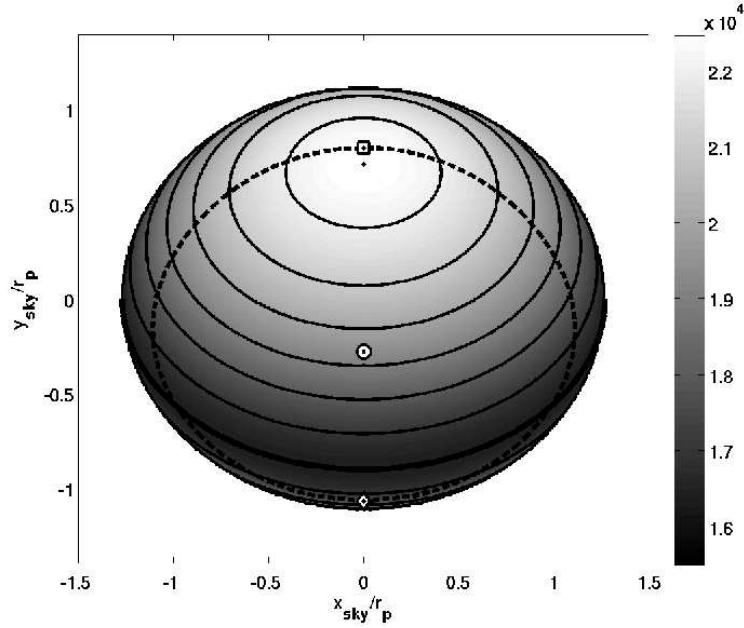


Fig. 2.— The temperature structure of a B2V star rotating at $v_{\text{frac}} = 0.8$ viewed with an inclination of 45° to the polar axis (marked by a small dot in uppermost oval). The bold, solid line is the equator. The local temperatures shown are determined by Equation (5). The dashed line is the limit of the region visible from a vantage point located within the disk at a radius of $s_R = 2r_p$ and a height of $s_z = 1.2r_p$, as defined by Equation (8). The square and diamond symbols mark the location of θ_1 and θ_2 respectively which are found by solving Equation (7). The direct line of sight from $s_R = 2r_p$ and $s_z = 1.2r_p$ is indicated by the symbol \odot .

If the equatorial radius expands with rotation, this can change the disk’s density structure if the R_* appearing in Equation 10 is associated with the star’s equatorial radius. This is undesirable because we wish to investigate changes in the disk temperatures resulting solely from the changing photoionizing radiation field seen by the disk and not from an unintended change to the underlying density structure of the disk. Unfortunately, there is no ideal solution to this complication and several approaches are outlined in Appendix A. In the notation of Appendix A, all of the calculations were computed with an unchanging grid in which the inner edge of the disk is set to $3/2 r_p$. This approach preserves the disk density structure and is best for temperature comparisons. A physical grid, in which the density structure of the non-rotating star is shifted outward as R_* increases, is more useful when calculating observables, and this grid will be used in a subsequent paper on predicted $H\alpha$ line profiles and infrared excesses.

Table 1: Adopted stellar parameters

Spectral Type	Mass (M_\odot)	Polar Radius (R_\odot)	Luminosity (L_\odot)	ω_{crit} (s^{-1})	$v_{\text{crit}} = \frac{3}{2} r_p \omega_{\text{crit}}$ (km s^{-1})
B0V	17.5	7.40	3.98×10^4	7.10×10^{-5}	548
B2V	9.11	5.33	4.76×10^3	8.38×10^{-5}	466
B3V	7.60	4.80	2.58×10^3	8.95×10^{-5}	449
B5V	5.90	3.90	7.28×10^2	1.08×10^{-4}	439

Notes: Stellar parameters adopted from Cox (2000).

Table 2: Adopted rotation rates and example equatorial speeds.

v_{frac}	ω_{frac}	r_{eq}/r_p	v_{eq} B0 (km s^{-1})	v_{eq} B3 (km s^{-1})	v_{eq} B5 (km s^{-1})
0.000	0.000	1	0	0	0
0.001	0.002	1.00	0.55	0.45	0.40
0.200	0.296	1.01	110	90	80
0.400	0.568	1.06	219	180	160
0.600	0.792	1.14	329	269	241
0.800	0.944	1.27	438	359	321
0.950	0.996	1.43	521	427	381
0.990	0.999	1.49	544	445	397

The photoionizing radiation field incident on the disk was calculated as follows: first, von Zeipel’s constant is found by using Equation 6 to rescale an interpolated value of C_ω from Collins (1966) to match the stellar parameters. Next, for each point in the disk, the visible region of the stellar surface is determined, and a grid is constructed across this surface. At each point in this surface grid, the local temperature, local gravity, and the viewing angle are found. Finally, the specific intensity, $I_\nu(T_{\text{eff}}, g)$, for each point is scaled from the Kurucz (1993) model atmosphere closest to the effective temperature and gravity at each location, $I_\nu^K(T_{\text{best}}, g_{\text{best}})$, to the required temperature using a blackbody function,

$$I_\nu(T_{\text{eff}}, g) = I_\nu^K(T_{\text{best}}, g_{\text{best}}) \frac{B_\nu(T_{\text{eff}})}{B_\nu(T_{\text{best}})}. \quad (11)$$

Here T_{eff} is the local effective temperature of the stellar surface, and T_{best} and g_{best} are the parameters of the closest matching Kurucz model. The available Kurucz grid of model atmosphere intensities was interpolated to a finer grid of spacing of $\Delta T_{\text{eff}} = 200\text{K}$ and $\Delta \log(g) = 0.10$. Equation 11 was used to correct the intensity only in these very narrow temperature bins.

Most of the calculations performed in this work implement the above description of gravitational darkening and are referred to as full gravitational darkening (FGD) calculations. All of the models presented in Section 4 are FGD calculations. However in Section 5, two simplified approaches are described which isolate one of the two main effects of gravitational darkening: spherical gravitational darkening (SGD), accounting only for the temperature change across the stellar surface, and pure shape distortion (PSD), accounting only for the changing the shape of the star.

4. Results for Gravitationally-Darkened Be Star Disks

4.1. Energy reaching the Circumstellar Disk

The stellar radiation field is modified by gravitational darkening, and this directly affects the disk temperatures through the photoionization rates. Figure 3 shows the total photoionizing mean intensity at each location in the computation grid for a B2 star both with and without a disk, and with and without rotation. The mean intensity ratios between the various cases are also shown. Consider the left-hand panels A and B in which there is no disk material. In the rotating case ($v_{\text{frac}} = 0.99$), less radiation from the poles reaches the equatorial regions of the disk, and this results in the hour glass shape in the mean intensity of panel B. In the bottom-left panel which gives the ratio of the rotating to non-rotating case, the stellar radiation field reaching the disk has been reduced by approximately 50%

compared to the non-rotating star. However, for regions close to the star and near the equatorial plane, there can be reductions as great as 90%. Now consider the right-hand panels C and D in which the opacity and emissivity of the disk gas have been included. Again the cases of rotation at $v_{\text{frac}} = 0.99$ and no rotation are compared. Most of the radiation reaching various positions within the disk is re-processed by the circumstellar gas between a particular location and the star. In general, the total irradiance reaching the shielded parts of the disk is reduced down with gravitational darkening by about 50%. However, there are locations within the mid-regions of the inner disk where the energy actually increases with rotation (see Figure 3) due to changes in the disk’s opacity.

4.2. Temperatures in the Circumstellar Disk

Any change in the energy received from the star produces a change in the radiative equilibrium temperature. The changes produced by increasing rotation on the general temperature structure of the disk are illustrated in Figures 4 through 7 for the spectral types given in Table 1. Shown in all figures are four disk temperature diagnostics: the maximum temperature, the minimum temperature, the density-weighted temperature, defined as

$$\bar{T}_\rho = \frac{1}{M_{\text{disk}}} \int T(R, z) \rho(R, z) dV , \quad (12)$$

and the volume-averaged temperature, defined as

$$\bar{T}_V = \frac{1}{V_{\text{disk}}} \int T(R, z) dV . \quad (13)$$

In order to avoid numerical effects, the maximum and minimum temperatures are averages over the twenty hottest and twenty coolest disk locations, respectively. In Figures 4 through 7, all of these temperature diagnostics are plotted as a function of v_{frac} and ω_{frac} . Because their behaviour depends somewhat on spectral type, the results for each model are discussed separately.

For the B0 model, seen in Figure 4, both the density and volumed-averaged disk temperatures decrease steadily with increasing rotation. Small declines in the density-weighted, maximum, and minimum disk temperatures are apparent even at $v_{\text{frac}} \approx 0.4$. By critical rotation, the density-weighted temperature has fallen to just under 11,000 K, a decline of 2500 K compared to the non-rotating case. The decline is not as large in the volumed-average temperature, and this is likely due to the influence of the hotter stellar pole that develops for increased rotation (see Figure 1); this is also reflected in the maximum and minimum disk

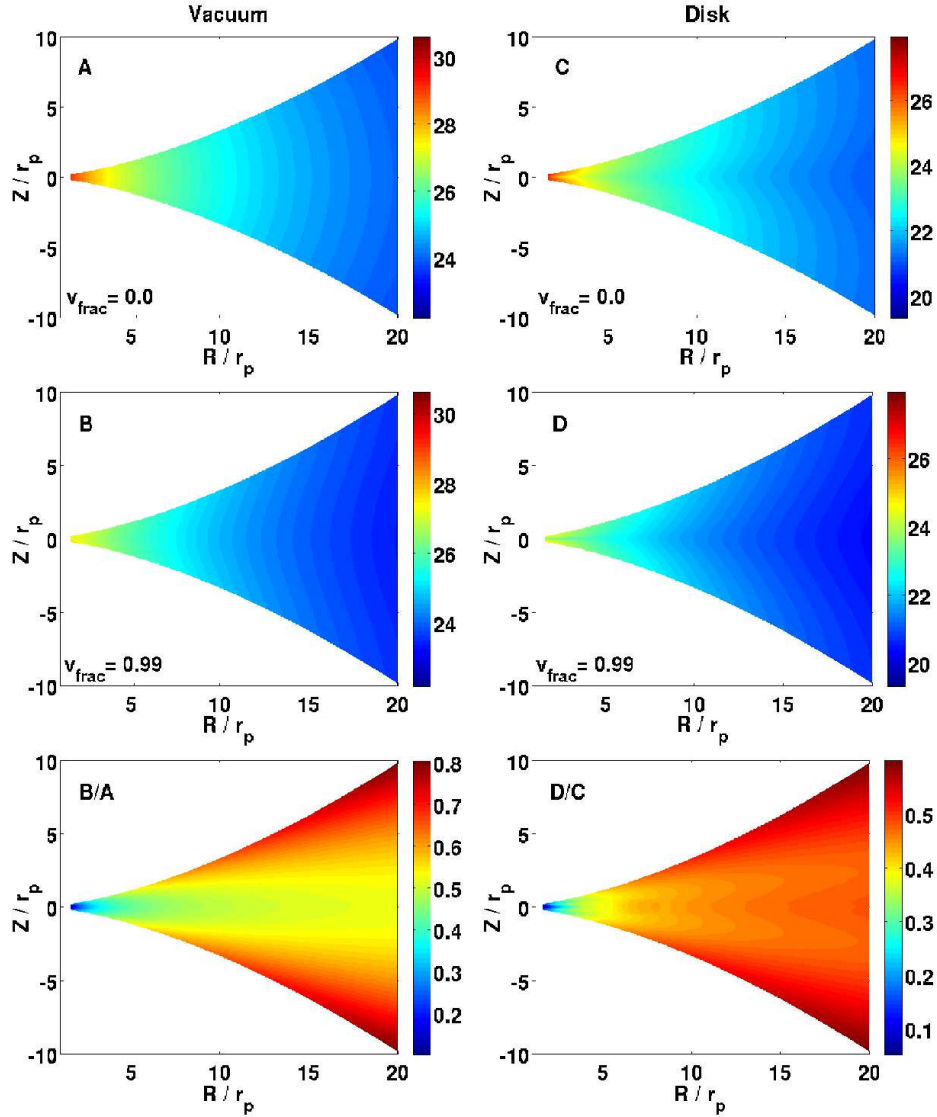


Fig. 3.— Left panels A and B show the log of the mean intensity at each location in the computational grid without any disk material present for a star with $v_{\text{frac}} = 0$ (panel A) and $v_{\text{frac}} = 0.99$ (panel B). The ratio of the mean intensity for the rotating case with the non-rotating case is given in the bottom left panel (labelled B/A). The right panels C and D show the mean intensity at each location in the disk including the opacity effects of the disk material for a star with $v_{\text{frac}} = 0$ (panel D) and $v_{\text{frac}} = 0.99$ (panel E). The ratio of the shielded rotating case with the non-rotating case is shown in bottom right panel (labelled D/C).

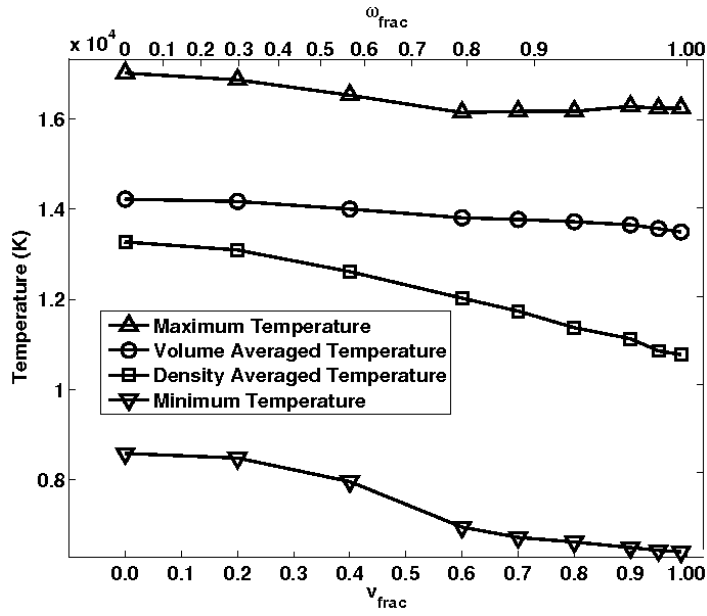


Fig. 4.— Change in disk temperature diagnostics with increasing rotation for the B0 model.

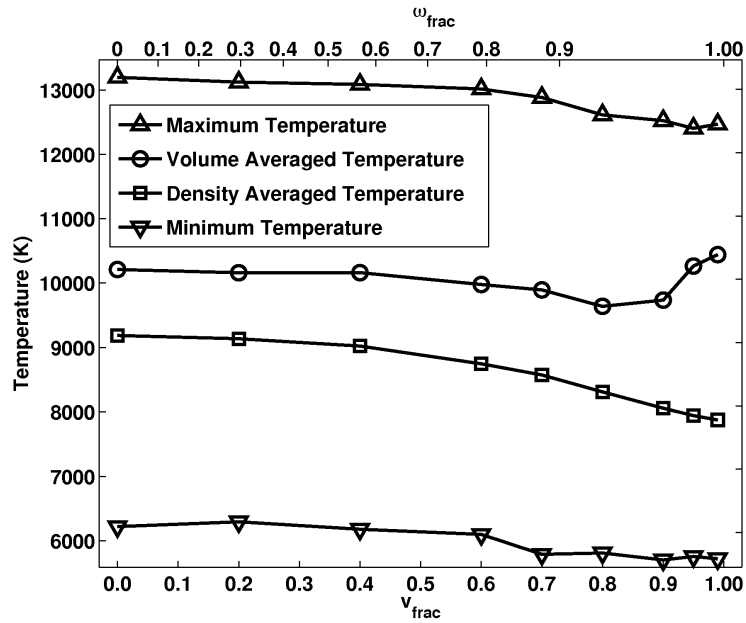


Fig. 5.— Same as Figure 4 for a B2 star.

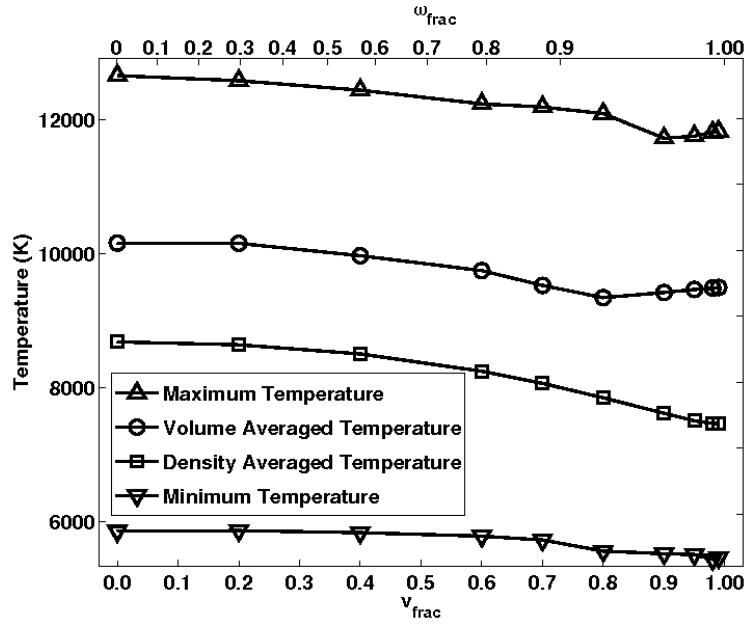


Fig. 6.— Same as Figure 4 for a B3 star.

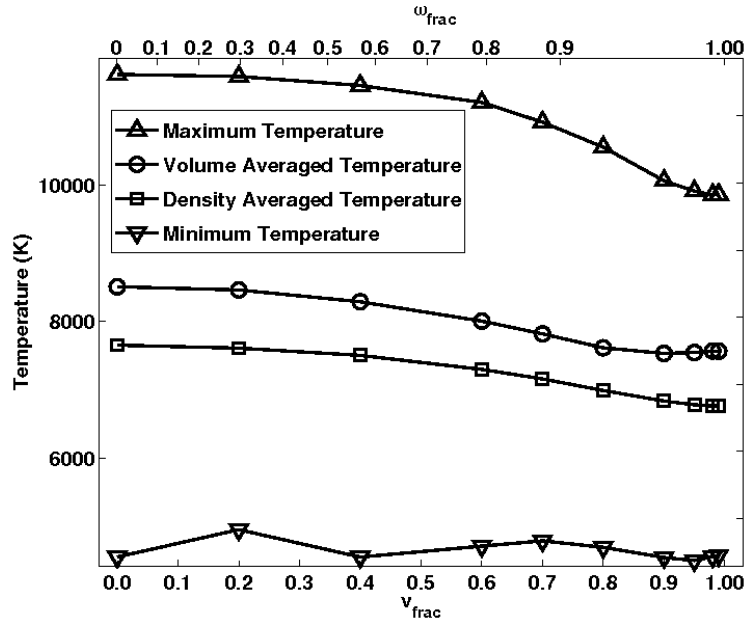


Fig. 7.— Same as Figure 4 for a B5 star.

temperatures: while the minimum temperature has a steep decline, the maximum temperature is much flatter and actually reaches a shallow minimum at an intermediate rotation rate.

For the B2 model, shown in Figure 5, all temperatures initially decline slowly. The density-weighted disk temperature falls from over 9000 K in the non-rotating case to under 8000 K by critical rotation. However, unlike the previous case, the volume-averaged temperature reaches a minimum near $v_{\text{frac}} \approx 0.8$ and then begins to increase for extremely rapid rotation. The lack of an increase in the density-weighted temperature indicates that the additional heating occurs mainly in the upper disk, where there is less gas, and the heating is likely due to the effect of the hot stellar pole. We also note that minimum temperature in the disk, ≈ 6000 K, is approximately constant with rotation, with only a small decline for $v_{\text{frac}} \geq 0.7$.

Spectral type B3 is shown in Figure 6. Its behaviour is very similar to the B2 case above, although the temperature rise in the volume-weighted average temperature above $v_{\text{frac}} \geq 0.8$ is not as large as in the B2 case. Again the minimum disk temperature is around 6000 K and is not strongly affected by rotation. For B5, shown in Figure 7, both the density and volume-averaged temperatures show a similar decline with rotation and there is no rise in the volume-averaged temperature above $v_{\text{frac}} \geq 0.9$. By this spectral type, the minimum disk temperature has fallen to ≈ 5000 K and shows no clear trend with rotation. The low temperatures reached in this model have implications for later spectral types that we shall now discuss.

As noted in the introduction to Section 3, we have not considered a model of spectral type B8 from the VL (very late) spectral bin of Cranmer (2005). Our test calculations have indicated that very cool disk temperatures are reached in this model, particularly for near critical rotation, and these may fall outside of the domain of applicability of the current version of BEDISK. In particular while the global density-weighted disk temperature still exceeds 6000 K for a B8 model, there is a significant volume of the disk which falls well below 5000 K by $v_{\text{frac}} = 0.99$. While our calculations include abundant metals with low ionization potentials (such as Mg, Ca, and Fe) that provide sources of free electrons at low temperatures, molecule formation is not included. In addition for such cool disks, the treatment of the diffuse radiation field generated within the disk may require a more careful treatment. For these reasons, we have chosen not to include B8 models in this work. We note that in the analysis of Cranmer (2005), the four bins we do account for include the full range of inferred threshold rotation rates, from $v_{\text{frac}} \approx 0.6$ for early spectral types B0–B2 to $v_{\text{frac}} \approx 1.0$ for the late spectral type B5.

The effect that near critical rotation ($v_{\text{frac}} = 0.99$) has on the global, density-weighted

disk temperature is summarized in Table 3. Compared to non-rotating models, near critical rotating models are between 15 and 20% cooler with the largest difference occurring for the earliest spectral type considered (B0).

Next we discuss how the detailed temperature structure of a Be star disk, $T(R, z)$, changes with rotation. In general, Be star circumstellar disks are highly non-uniform in temperature as disks of sufficient density develop a cool, inner zone surrounded by a larger warm region (Millar & Marlborough 1998; Sigut et al. 2009). Between these two regions is the hottest part of the disk, forming a narrow sheath. Figures 8 and 9 show the effect of rotation on the temperature of disks surrounding stars of spectral types B0 and B5 respectively. In each plot, temperature distributions for two models are shown, one with $v_{\text{frac}} = 0.0$ and the other with $v_{\text{frac}} = 0.95$. Also shown is the temperature difference between the rotating and non-rotating models and a histogram of these differences. The value of $v_{\text{frac}} = 0.95$ was chosen for the rotating model because this is approximately the rotation rate required for a velocity perturbation on the order of the local sound speed in the star’s photosphere to be sufficient to feed material into a rotationally supported disk.

For the B0 model, shown in Figure 8, the most dramatic changes in temperature occur because of the expansion of the cool, inner zone to larger radii with increased rotation. In the non-rotating case, this cool region does not extend past $\approx 7 R_*$ while in the $v_{\text{frac}} = 0.95$ model, it extends well past $10 R_*$. This results in some computational grid points that are more than 4,000 K cooler in the rotating model (compared to the 2500 K difference in the density-weighted average) as illustrated by the histogram of temperature differences in Figure 8. However, there are also temperature changes in the hot sheaths above and below the inner cool zone close to the star. For the $v_{\text{frac}} = 0.95$ model, these hot sheaths occur only beyond $\approx 3 R_*$ whereas in the non-rotating case, these sheaths extend to the inner edge of the disk.

Table 3. Change in density-weighted average disk temperature for near-critical rotation.

Spectral Type	$\overline{T}_\rho(K)$		% Change
	$v_{\text{frac}} = 0.00$	$v_{\text{frac}} = 0.99$	
B0	13280	10780	-19
B2	9190	7870	-14
B3	8690	7460	-14
B5	7660	6760	-12

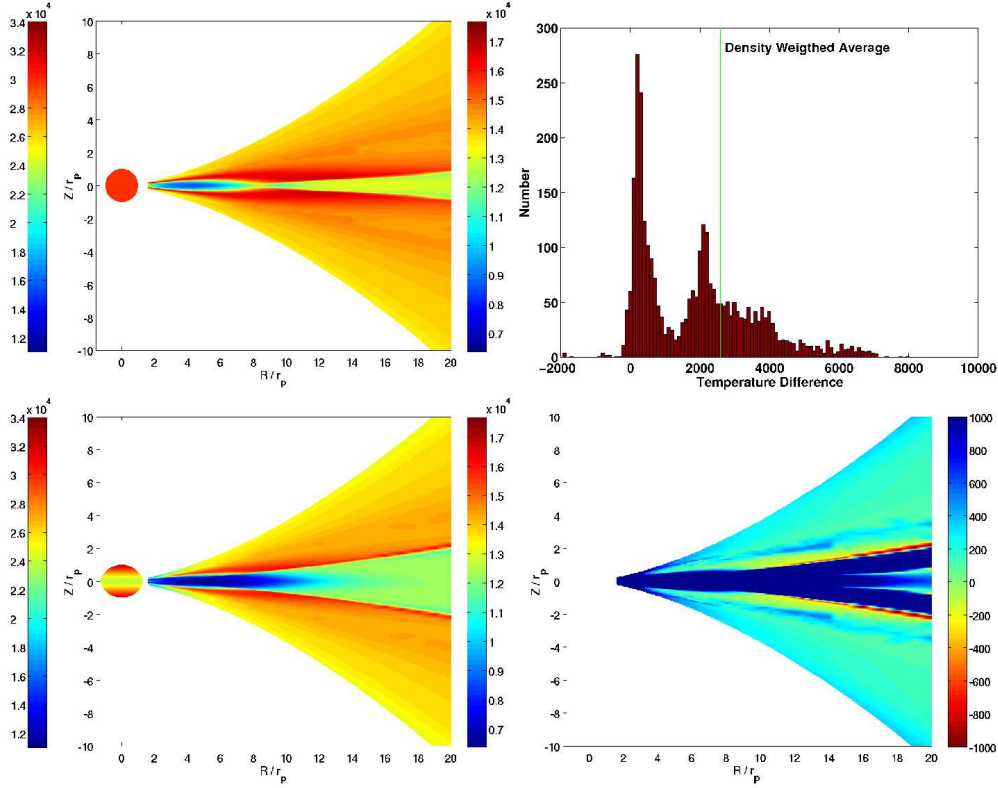


Fig. 8.— Temperatures for both a non-rotating B0 star and its circumstellar disk (upper left) and a B0 star rotating at $v_{\text{frac}} = 0.95$ with an identical disk (lower left). In each of these panels, the colour bar on the left is for the star and the colour bar on the right, for the disk. The lower right panel shows the temperature differences in the disk. Positive differences mean that the non-rotating star is hotter. The upper-right panel shows a histogram of the temperature differences.

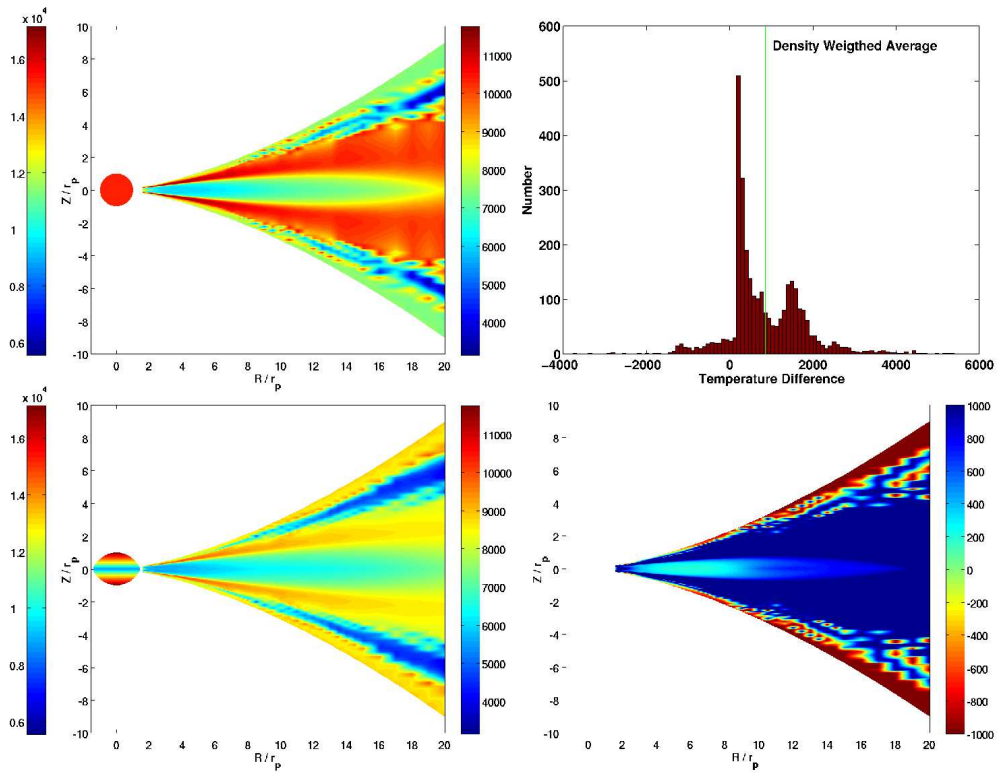


Fig. 9.— Same as Figure 8 for a B5 star.

Despite these changes, the temperature in the equatorial plane of the cool, inner zone does not drop dramatically with rotation, likely due to the high optical depths along the rays back to the star. This explains why the density-weighted average temperature of the disk shows only a modest decrease compared to the non-rotating case (see Figure 4). Interestingly, the rotating model is actually hotter than the non-rotating model in a narrow region a few scale heights above the equatorial plane for $R > 10R_*$, although the number of computational grid points involved is quite small. The optically thin gas above and below the plane of the disk shows only a very small decrease in temperature and thus the volume-averaged temperature of Figure 4 is essentially unaffected by rapid rotation.

Figure 8 clearly illustrates that the temperature distribution surrounding a rotating star may differ dramatically from the non-rotating case, even when global measures of disk temperature such as \bar{T}_ρ and \bar{T}_V are similar. From the point of view of computing the strength of emission lines or the infrared excess, the increased extent of the inner cool zone and the changes to the temperature of the hot sheaths above and below this zone have the potential to produce large changes in these observational diagnostics. Such changes will be discussed in a subsequent paper.

Figure 9 shows a similar comparison between a non-rotating model and one rotating at $v_{\text{frac}} = 0.95$ for spectral type B5. As in the B0 case, the main effect is the extension of the inner, cool zone to larger radii. However the B5 model also has a significant extension of this cool zone to larger distances above (and below) the plane of the disk. As these regions occupy a significant volume, the volume-weighted disk temperature is significantly decreased (unlike the previous case of a B0 star). As shown in Figure 7, both the density and volumed-weighted disk temperatures show a similar drop with rotation.

While most disk locations are, as before, cooler, there is a much larger fraction of disk locations that are hotter in the B5 rotating model than in the previous B0 case. Most of these hotter regions are associated with a cool zone at large radii, $R > 10 R_*$, far above (and below) the equatorial plane of the disk. In these regions, the lines of sight back to the central star have significant optical depths whereas the optical depths (in the z -direction) to the nearest disk edge have become less than unity. Hence heating via photoionization is suppressed whereas cooling via escaping line radiation becomes effective and there is a reduction in temperature due to this cooling. This low temperature zone disappears for higher z because the optical depths back to the central star eventually drop and the heating rate increases. The exact location and detailed form of the zones is influenced by rotation and some locations with significantly hotter temperatures are predicted. It should be kept in mind that at large radii and far above or below the plane of the disk, the gas densities are very low, and the detailed structure of these cool zones will have little effect on observable

diagnostics such as emission line strengths, polarization, or infrared excess.

While the detailed $T(R, z)$ comparisons of the previous paragraphs are instructive, it is difficult to see general trends over a wide range of rotation rates. For this reason, it is useful to have temperature diagnostics that are intermediate between the disk-averaged, global measures of Figures 4 to 7 and the detailed temperature distributions of Figures 8 and 9. To this end, we have performed both vertical (z) and radial (R) temperature averages over the disks of three stellar models (B0, B3, and B5) and considered how these averages are affected by a wide range of rotation rates.

The vertical temperature averages (yielding an average disk temperature as a function of distance from the star) were computed via

$$\bar{T}(R) = \frac{\int_0^{z_{\max}} T(R, z) \rho(R, z) dz}{\int_0^{z_{\max}} \rho(R, z) dz}, \quad (14)$$

and the change in vertically-averaged, density-weighted temperature as a function of radius is shown in Figures 10 through 12 for three stellar models, B0, B3, and B5. Five rotation rates, $v_{\text{frac}} = 0.00, 0.40, 0.80, 0.90, 0.95$ and 0.99 , were considered. The behaviour of the B2 model of Table 1, not shown for brevity, is similar to the B3 case. In all cases considered, the $v_{\text{frac}} = 0.40$ models show vertically averaged temperatures that are very close to the non-rotating case while significant differences develop by $v_{\text{frac}} = 0.80$.

These vertical averages show that the region next to the central star is hottest, followed by a rapid decrease towards a minimum temperature near $\approx 4 R_*$ (for B0) to $\approx 6 R_*$ (for B5). Further out, the temperature increases again towards the outer region of the disk. In the B0 model, the temperature then plateaus, whereas in the B3 and B5 models the temperature is still increasing by $R \approx 20 R_*$. From these figures, it can be seen that increasing rotation tends to: (1) decrease the average temperature at all radii, (2) move the location of the temperature minimum in the cool zone inward (although not in the B0 model), and (3) broaden the extent of the cool, inner zone. Rotation also tends to flatten the temperature increase occurring in the outer regions of the disk.

Turning to the vertical (z) structure of the disks, we define a density-weighted, radially-averaged temperature (yielding an average temperature as a function of height above the equatorial plane) as

$$\bar{T}(u) = \frac{\int_0^{R_{\max}} T(R, u) \rho(R, u) A(R, u) dR}{\int_0^{R_{\max}} \rho(R, u) A(R, u) dR}, \quad (15)$$

where $u \equiv z/H(R)$ and $H(R)$ is the vertical scale height given by Equation 10. The vertical variable, z , was rescaled by $H(R)$ because lines of constant u better define a radial average due to the increase in the disk scale height with R (see Equation 10). The function $A(R, u)$

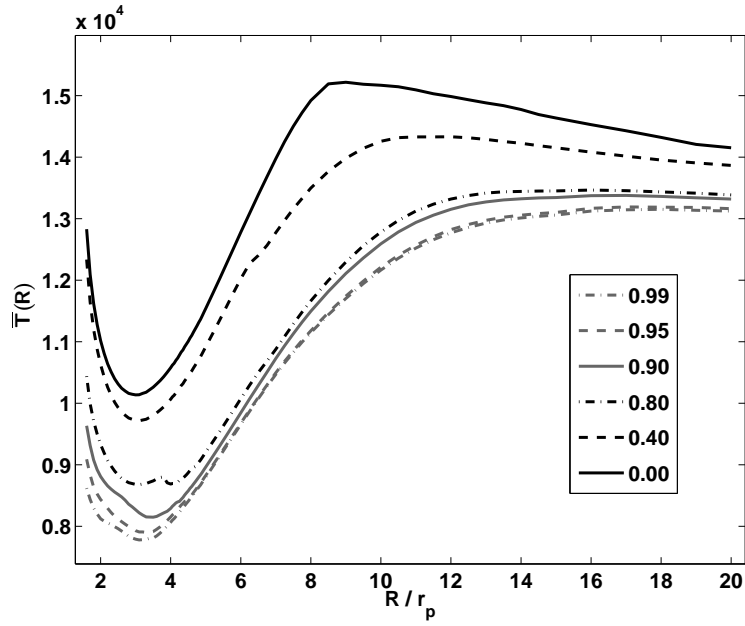


Fig. 10.— Variation of the vertically-averaged, density-weighted temperature with disk radius for various stellar rotation rates for the B0 model.

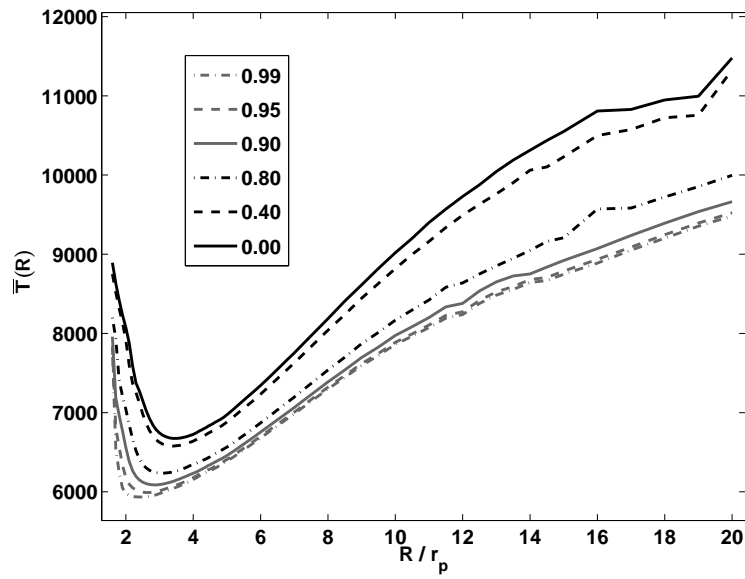


Fig. 11.— Same as Figure 10 for the B3 model.

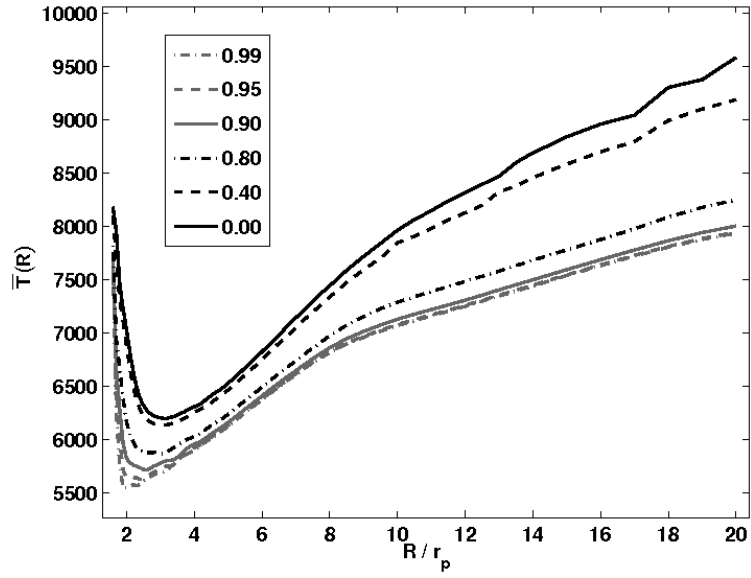


Fig. 12.— Same as Figure 10 for the B5 model.

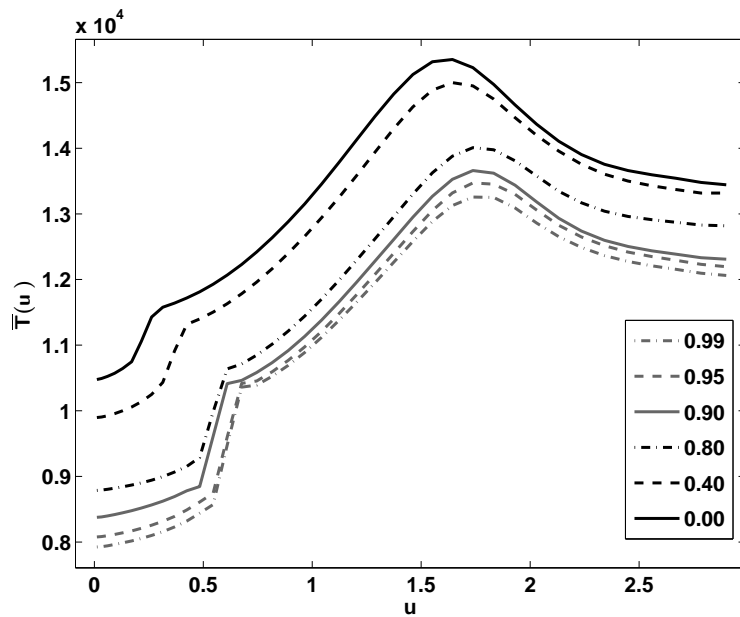


Fig. 13.— Variation of the radially averaged temperature profile in the vertical direction for the B0 model. Here the gas scale height is the variable u defined by $u \equiv z/H(R)$.

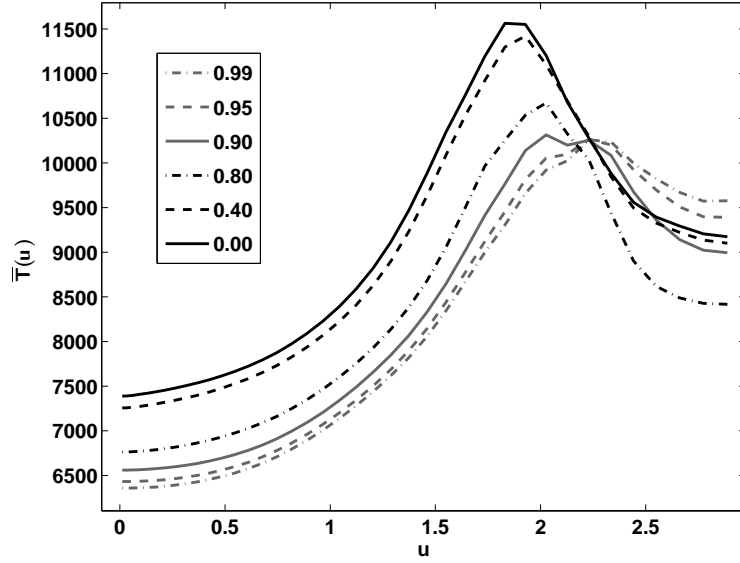


Fig. 14.— Same as Figure 13 for the B3 model.

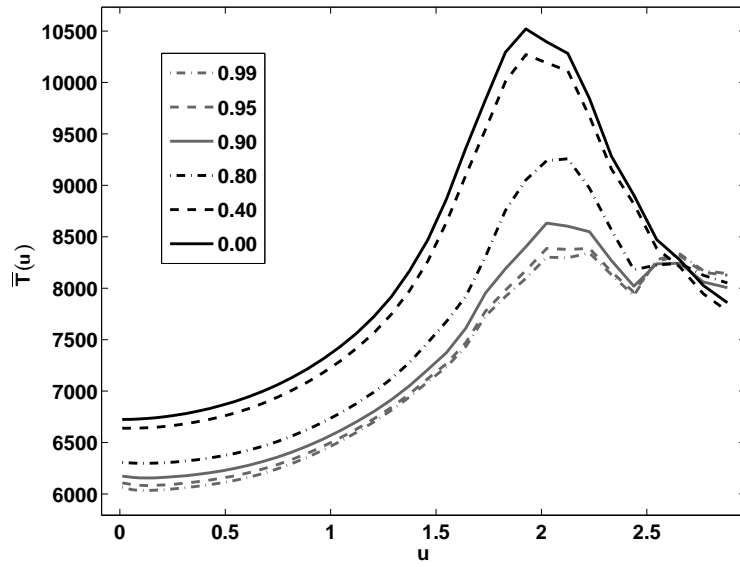


Fig. 15.— Same as Figure 13 for the B5 model.

arises because Equation 15 is effectively a line integral through the computational grid. At each R_i in the discrete sum used to compute this integral, z must be found from R_i and the required u . As different z occur in the sum and the spacing of the z -grid increases with R , we have weighted each z point by the width of the strip it effectively represents as based on the local grid spacing; this is the origin of the $A(R, u)$ function. Such considerations do not occur for Equation 14 because this integral is performed over all z_j for a *fixed* R_i .

The changes in the vertical temperature structure with rotation are shown in Figures 13 through 15 for spectral types B0, B3, and B5, respectively. Again, the B2 model of Table 1 is similar to B3 but is not shown for brevity. Note that for each spectral type, the set of weights $A(R, u)$ used in Equation 15 is always the same as the computational grid is fixed and independent of v_{frac} (i.e. we have chosen to use the unchanging grid of Appendix A).

In general with increasing vertical height (i.e. perpendicular to the equatorial plan), the temperature is coolest in the plane of the disk ($z = 0$) and then rises to a maximum near $u \approx 2$. This maximum corresponds to the hot sheath seen in the plots of the temperature distributions in these disks (for example, see Figure 8). At larger heights, the temperature drops below the mid-plane maximum and is nearly constant. With increasing rotation, several trends are seen: (1) rotation reduces the temperature at all scale heights, (2) rotation increases the vertical extent of the cool, inner zone, (3) rotation decreases the temperature maximum in the mid-plane, and (4) rotation shifts the maximum temperature to larger scale heights, although this shift is not large.

Nevertheless, there are exceptions to these general trends, particularly in the temperatures at large u . In the B0 model (Figure 13), the temperature at the upper edge of the disk decreases monotonically with rotation. However, for the B3 model, the temperature at the upper edge of the disk is actually largest for the greatest rotation rate. The location of the hot sheath (the temperature maximum in u) moves outward in u for later spectral types; it occurs well below $u = 2$ for the B0 model at all rotation rates, whereas it is above $u = 2$ for the two later spectral types, and it moves higher with increased rotation. Hence in the later spectral types, the temperature at the upper edge of the disk is affected by the presence of the hot sheath.

Finally, turning back to global measures of disk temperature, Figure 16 summarizes the change in the density-weighted average disk temperature with rotation for all four spectral types. In general, the non-rotating models define the upper envelope of the temperatures while the extreme rotators ($v_{\text{frac}} \geq 0.95$) define the lower temperature envelope. In constructing this figure, any change in the overall spectral type of the star due to increasing rotation has been ignored.

5. Approximate Treatments of Gravitational Darkening

In this section, we assess the effectiveness of partial or approximate treatments of gravitational darkening. In one approach, spherical gravitational darkening (SGD), we have treated the star as a sphere and implemented only the variation of the photospheric temperature across the stellar surface. As this procedure is very simple to implement, it is of interest to see how the predicted disk temperature structure compares to the full treatment. In another approach, pure shape distortion (PSD), we include only the rotational distortion of the central star, and not the temperature variation, to understand the effects of geometry alone. Global density and volume-weighted disk temperatures for both approximations (SGD and PSD), and the full treatment (FGD), are shown in Figure 17 for the B2 stellar model.

The differences between FGD and SGD are subtle for $v_{\text{frac}} \leq 0.7$, with only small differences in the density-weighted and volume-weighted average temperatures. For the largest rotational rates, $v_{\text{frac}} \geq 0.95$, SGD predicts density-weighted temperatures that level off for higher rotation rates while the full treatment gives temperatures that continue to drop. The difference amounts to $\approx +500$ K for the SGD model at $v_{\text{frac}} = 0.99$ in the density-weighted average temperature. In the volume-averaged temperature, the FGD temperature actually falls below the SGD prediction in the vicinity of $v_{\text{frac}} \approx 0.80$, but then increases above the SGD prediction for larger rotation rates. By $v_{\text{frac}} = 0.99$, the difference is again about 500 K.

To further illuminate this result, these calculations were repeated with PSD. As evident from Figure 17, PSD results in essentially no change to the average disk temperatures for $v_{\text{frac}} \leq 0.7$ and only very small changes for faster rotation rates. This, of course, does not mean that the effect of the rotational distortion of the stellar surface is unimportant; indeed the difference between the FGD treatment and SGD noted above is the neglect of the stellar distortion. The PSD treatment simply illustrates that the distortion of the stellar alone produces almost no change in global disk temperatures.

However global temperature diagnostics tell only part of the story. To illustrate how the temperature structure of the disk is reproduced by the SGD approximation, Figure 18 compares the vertically-averaged (Eq. 14) and radially-averaged (Eq. 15) disk temperatures for a B2 stellar model computed with three rotation rates, $v_{\text{frac}} = 0, 0.80, \text{ and } 0.95$. As can be seen from the Figure, there are significant differences between all the rotating models (either FGD or SGD) and the non-rotating model, and all of the previously discussed effects can be seen. Interestingly both SGD profiles for $v_{\text{frac}} = 0.8$ are close to the FGD prediction. However by $v_{\text{frac}} = 0.95$, the SGD temperature profiles remain close to the $v_{\text{frac}} = 0.8$ SGD predictions and do not follow the trend of the full (FGD) treatment; this is particularly

noticeable in the radially-averaged profile (bottom panel) where the (average) location of the hot sheath is very poorly predicted by the SGD model. We conclude that SGD is an acceptable approximation to the temperature structure only for $v_{\text{frac}} \leq 0.8$, and that for higher rotation rates, the full treatment is required.

6. Conclusions

Gravitational darkening produces noticeable changes in the temperature structure of Be star circumstellar disks. Rotation causes the stellar surface temperature to diverge from a single value into a range of temperatures, and this changes the photoionizing radiation field incident on the disk. Three measures of disk temperature were used to quantify the effect of rapid rotation: detailed temperature distributions, $T(R, z)$, vertically and radially-averaged disk temperatures, and global density or volumed-weighted average disk temperatures that reduced the complex temperature variations of the disk to a single, average temperature. Among these choices, the vertically and radially-averaged temperatures are perhaps the most useful for illustrating the effect of rapid rotation over a wide range of rotation rates and spectral types.

Rapid rotation of the central star and the accompanying gravitational darkening cause most of the disk gas to systematically decrease in temperature, and this is reflected in lower density-weighted, average disk temperatures for increasing rotation rates. However volume-averaged disk temperatures indicate that upper regions of the disks can experience additional heating at rotational speeds above 80% of the critical rate. Such changes cannot be produced by simply lowering the effective temperature of the star with rotation.

All spectral types considered, B0–B5, show a decline in the global, density-weighted averaged disk temperature of ≈ 15 –20% for near critical rotation. The decline is largest for the earliest spectral type considered, B0. Changes in the global, volume-weighted average disk temperature and the minimum and maximum temperatures in the disk also occur, although results are dependent on spectral type. The volume-weighted average temperature shows the effect of the hot stellar pole (that develops for rapid rotation) at intermediate spectral types B2 – B3 (see Figures 5 and 6).

The most important change to the temperature structure of the disks is the expansion of the inner cool, zone close to the central star. This zone develops in all disks of sufficient density, and this cool region generally expands in both radius and height as the rotation rate is increased. Also important are the hot sheaths above and below the cool, inner zone. These generally decrease in temperature and move to larger scale heights with increased rotation.

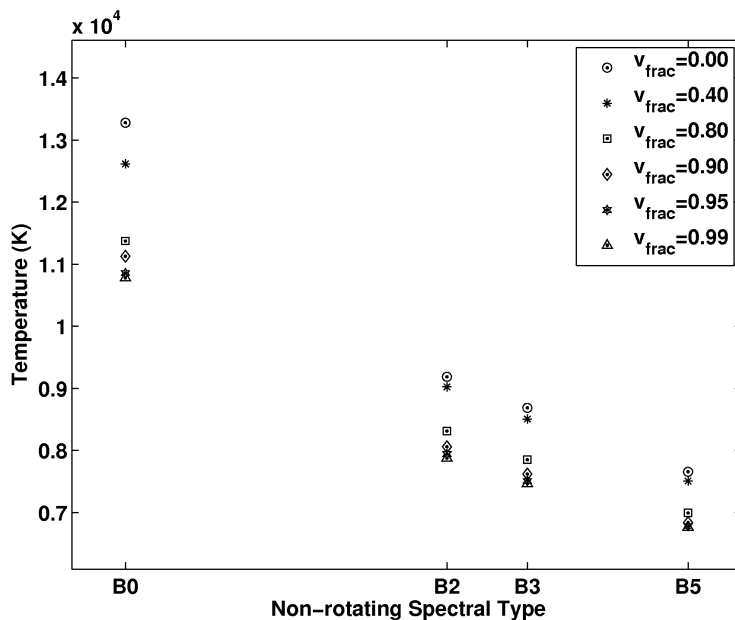


Fig. 16.— Density-weighted temperature average plotted against spectral type for six different rotation rates.

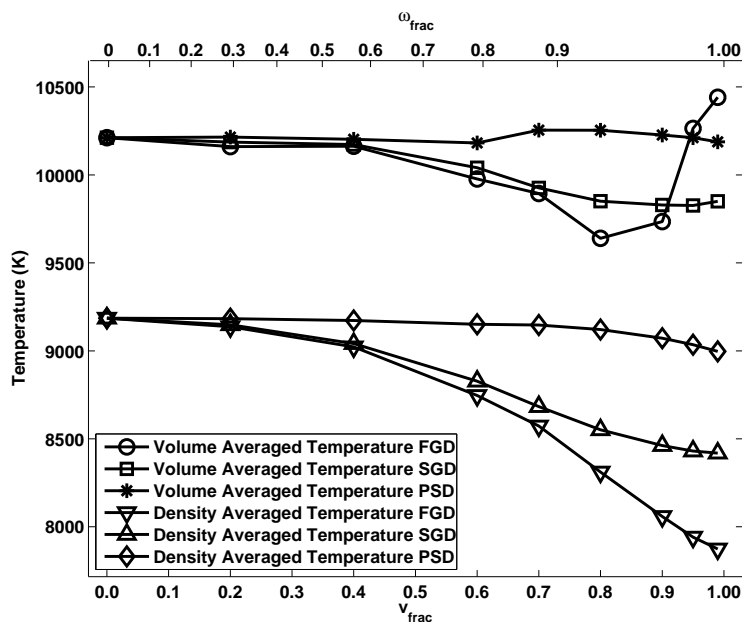


Fig. 17.— The global volumed-averaged and density-averaged disk temperature as a function of v_{frac} for the B2 model. Three different treatments of gravitational darkening considered: FGD, SGD, and PSD.

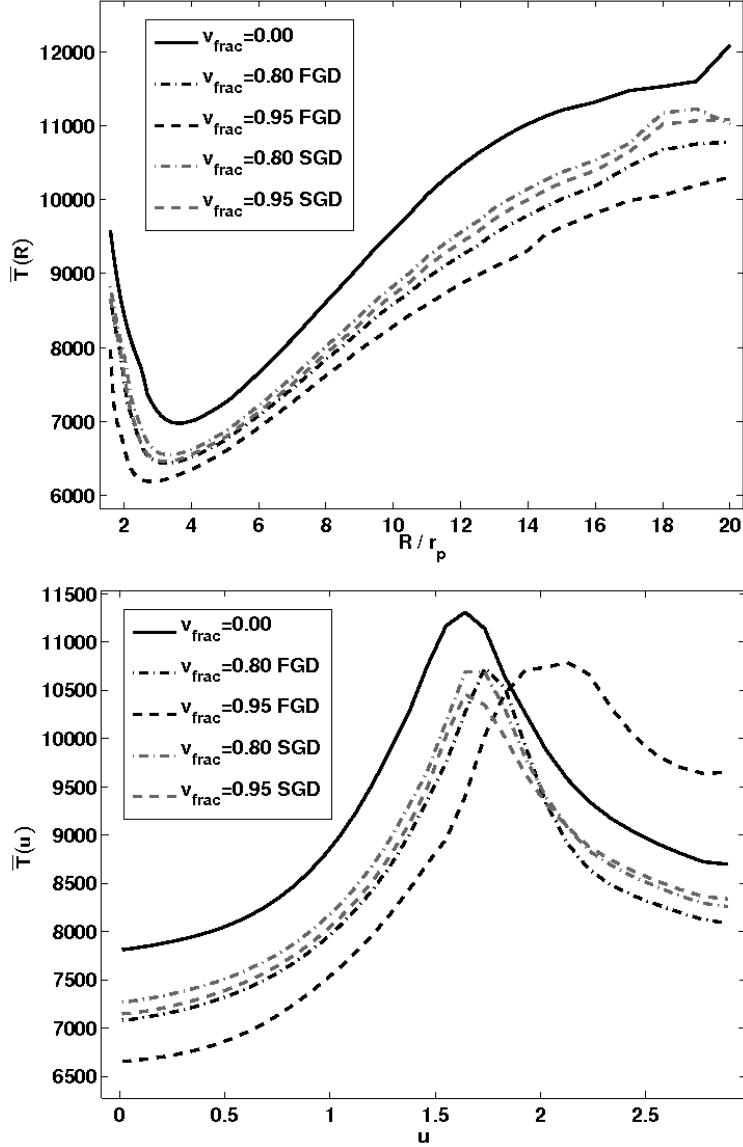


Fig. 18.— Vertically-averaged (top panel) and radially-averaged (bottom panel) temperature profiles (see Equations 14 and 15) for a B2 stellar model that compare the SGD approximation with the full treatment (FGD). Models rotating at $v_{\text{frac}} = 0$ (solid lines), 0.80 (dot-dashed lines) and 0.95 (dashed lines) are shown.

It is these complex changes that will most affect physical observables such as the H α emission line strength or the infrared excess. These issues will be explored in a subsequent paper.

The temperature effects of gravitational darkening on global measures of Be star circumstellar disks can be adequately approximated by spherical gravitational darkening (SGD, which ignores the distortion of the stellar surface) for rotation rates less than 80% of critical. For higher rotation rates, the distortion of the stellar surface must be included to accurately compute the disk’s global average temperature. Comparisons of the vertically-averaged and radially-averaged disk temperature profiles for models with different rotation rates suggests that the general temperature structure of the circumstellar disk can be reasonably predicted using the SGD approximation for rotation rates of also less than 80% of critical.

While the effect of rapid rotation of the central star can produce complex effects in the temperature structure of Be star circumstellar disks, temperature is, of course, not directly accessible to observers. In a subsequent paper, we will quantify the effect of rapid stellar rotation on the classic diagnostics of circumstellar material, namely emission line strengths and profiles and the predicted near-IR excess in the system’s spectral energy distribution.

We would like to thank the referee for many helpful comments. This research was supported in part by NSERC, the Natural Sciences and Engineering Research Council of Canada. MAM acknowledges the receipt of an Ontario Government Scholarship that funded part of this work.

REFERENCES

- Carciofi, A. C., Okazaki, A. T., Le Bouquin, J.-B., et al. 2009 *A&A*, 504, 915
- Carciofi, A. C., Domiciano de Souza, A., Magalhães, A. M., Bjorkman, J. E., & Vakili, F. 2008 *ApJ*, 676, L41.
- Domiciano de Souza, A., Kervella, P., Jankov, S. et al. 2003, *A&A*, 407, L47
- Chauville, J., Zorec J., Ballereau, D., et al. 2001, *A&A*, 378, 861
- Collins, G.W. II 1966, *ApJ*, 146, 914
- Coté, J., & Waters, L. B. F. M. 1987 *A&A*, 176, 93
- Cox, A.N. 2000, *Allens Astrophysical Quantities* (4th ed.; New York: Springer)
- Cranmer, Steven R. 2005 *ApJ*, 634, 585
- Dougherty, S. M., & Taylor, A. R. 1992 *Nature*, 359, 808
- Fremat Y., Zorec, J., Hubert, A.M., & Floquet M. 2005, *A&A*, 440, 305
- Hummel, W., & Vrancken, M. 2000, *A&A*, 359, 1075
- Kurucz, R. F. 1993, Kurucz CD-ROM No. 13. Cambridge, Mass: Smithsonian Astrophysical Observatory
- Lovekin C. C., Deupree, R.G., & Short, C. I. 2006 *ApJ*, 643, 460
- McLean, I. S., & Brown, J. C. 1978, *A&A*, 69, 291
- Maeder, A., & Meynet, G. 2000, *A&A*, 361, 101
- Meynet, G., Georgy, C., Revaz, Y., Walder, R., Ekström, S., & Maeder, A. 2010 in *The Interferometric View of Hot Stars*, *RevMexAA* (Serié de Conferencias), vol. 38, Th. Rivinius & M. Curé (eds), 113
- Millar, C.E., & Marlborough, J.M. 1998 *ApJ*, 494, 715

- Monnier, J.D., Zhao, M., Pedretti, E. et al. 2007, *Science*, 317, 342
- Owocki, S.P., Cranmer, S.R., & Blondin, J. M., 1994 *ApJ*, 424, 887
- Oudmaijer, R. D., Parr, A.M., Baines, D., & Porter, J.M. 2008 *A&A*, 489, 627
- Poeckert, R., Bastien, P., & Landstreet, J. D. 1979, *AJ*, 84, 812
- Porter, J. M. 1996, *MNRAS*, 280, L31
- Porter, J. M., & Rivinius, T. 2003 *PASP*, 115, 1153
- Sigut, T. A. A., & Jones, C. E. 2007 *ApJ*, 668, 481
- Sigut, T. A. A., McGill, M.A., & Jones, C. E. 2009, *ApJ*, 699, 1973
- Stee, Ph., & Bittar, J. 2001, *A&A*, 367, 532
- Tassoul, J.-L. 2000, *Stellar Rotation* (Cambridge: Cambridge University Press)
- Tycner, C., Lester, J. B., Hajian, et al. 2005, *ApJ*, 624,359
- Townsend, R. H. D., Owocki, S. P., & Howarth, I. D. 2004, *MNRAS*, 350, 189
- van Belle, G. T. 2010 in *The Interferometric View of Hot Stars*, *RevMexAA (Serié de Conferencias)*, vol. 38, Th. Rivinius & M. Curé (eds), 119
- Vinicius, M.-M. F., Townsend, R. H. D., & Leister, N. V. 2007 in *Active OB Stars: Laboratories for Stellar and Circumstellar Physics*, *ASP Conf. Ser. Vol. 361*, S. Štefl, S. P. Owocki and A. T. Okazaki (eds), 518
- Waters, L. B. F. M., Coté, J., & Lamers, H. J. G. L. M. 1987, *A&A*, 185, 206
- Zhao, M., Monnier, J. D., Pedretti, E. et al. 2010 in *The Interferometric View of Hot Stars*, *RevMexAA (Serié de Conferencias)*, vol. 38, Th. Rivinius & M. Curé (eds), 117

A. Construction of the Computational Grid

The primary goal of this paper is to explore changes in the thermal structure of a circumstellar disk caused by changes in the stellar flux due to rotation. Ideally the only difference between different models should be the rotation speed of the star. Rapid rotation has two effects on the central star; the dependence of the photospheric temperature on stellar latitude, and the Roche distortion of the stellar surface. If the latter effect (distortion) did not occur, creating a series of comparison models would be a simple matter of swapping out the central star and examining the corresponding changes in the thermal structure of the disk. Indeed, this is what occurs in the SGD approximation. Nevertheless, the stellar surface is distorted by rotation, and this geometrical change can be propagated into the physical properties of the disk. The simple fact that the distance between the stellar pole and equator changes with rotation is the central issue. For a given point within the disk it is possible to preserve the distance to one, but not both of these locations. Given this, there are several different ways one could attempt to mitigate the effects, and these approaches are discussed in this Appendix. All of the various choices are illustrated in Figure 19 which shows in the left hand panels, a non-rotating B2 star and its associated (R, z) grid and in the right hand panels, a B2 star rotating at $v_{\text{frac}} = 0.99$ and its associated (R, z) grid. In each panel, the (R, z) grid points in the circumstellar disk are shown as small dots.

In the most straight forward description, the grid locations (R, z) within the disk are specified in terms of the equatorial radius. In the absence of rotation, this is same as the polar radius. However when r_{eq} increases due to rotational distortion, the computation grid is stretched in both R and z (see Eq. 10). This increases the volume and mass of the disk. The computational grid points are also moved further from both the stellar pole, the stellar equator, and each other, as rotation increases. Hence with grids constructed in this way, any comparison between global temperature averages and total emission for increasing rotation must be considered carefully. Because of the simplicity of this approach, it will be referred to it as the naive grid. It is illustrated in panels A and B of Figure 19.

A simple alternative would be to define the grid spacing and density structure to be that of an non-rotating star, keep the grid fixed, and then shift the whole grid and density structure outward as r_{eq} increases. This preserves the distances of all grid points from the stellar equator and between each other. While the cross-sectional area and density structure remains unchanged, both the inner and outer radii of the disk are systematically increased causing the volume and mass of the disk to also increase with rotation. This effect can be noticed when the disk emission measure is calculated. The distance to the pole of the star also increases systematically with rotation, and this could bias any global temperature averages to lower temperatures. This approach will be referred to as the physical grid and

is illustrated in panels C and D of Figure 19.

An alternative to maintaining the distance between the grid points and the equator is to maintain the distance between grid points and the polar axis. Once again the grid spacing and density structure is defined to be that of a non-rotating star, but instead of shifting it outward as r_{eq} increases we simply remove sections of the grid that would be swallowed by the star and leave the rest of the disk unchanged. Unfortunately, the inner region which gets swallowed is also the densest region of the disk. More of this region is removed as rotation increases, and this systematically reduces all optical depths within the disk which in turn increases the stellar flux reaching the outer regions. This approach will be referred to as the swallowed grid and is illustrated in panels E and F of Figure 19.

One potential solution to the swallowed grid is to start the disk at $R = (3/2)r_p$ which allows the central star to swell to the inner disk boundary by critical rotation; the disk remains truly unchanged. This preserves disk volume, mass and density structure, and keeps the distances between each grid point and the stellar pole, the hottest part of the star unchanged. However, the distances to the stellar equator still systematically change. We call this the unchanging grid and it is illustrated in panels G and H of Figure 19. This method, unfortunately, makes important regions of the disk empty that were previously full and while comparisons between runs are unbiased any comparison to previous work becomes difficult. The dense inner region of the disk is the source of the IR lines and a significant amount of the mass in this region is no longer included.

In conclusion, there are four ways to define a grid surrounding an expanding star: a naive approach where everything increases, a physical grid which shifts the disk, a swallowed grid in which mass is lost from the disk; and an unchanging grid in which the star closes an inner gap. The results included in this paper were computed with the unchanging grid to allow the most straightforward temperature comparisons between the difference models.

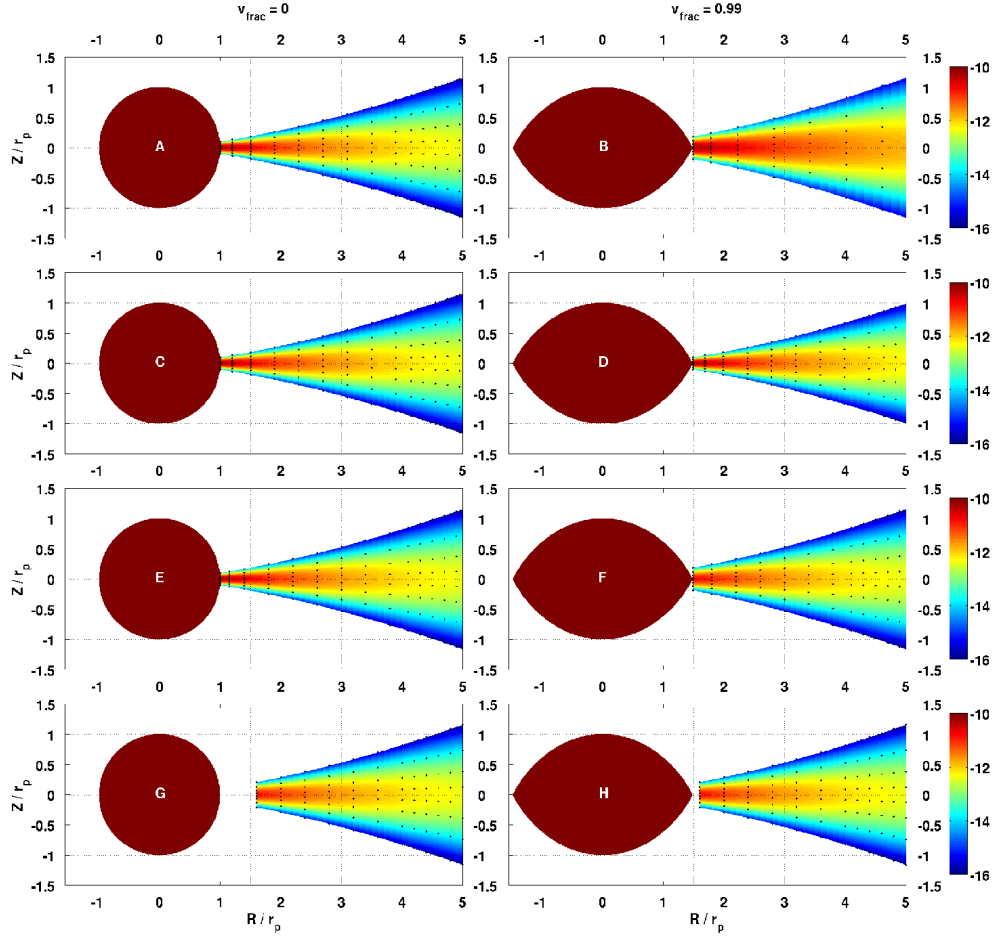


Fig. 19.— Each panel shows a cross section of the disk with the (R, z) grid points shown as small dots. The spherical star is not rotating, and the distorted star is rotating at $\omega_{\text{frac}} = 0.99$. Panels A and B depict the naive grid, panels C and D, the physical grid, panels E and F, the swallowed grid, and G and H, the unchanging grid. The colours represent the log of the disk density.